INDEX COPERNICUS INTERNATIONAL

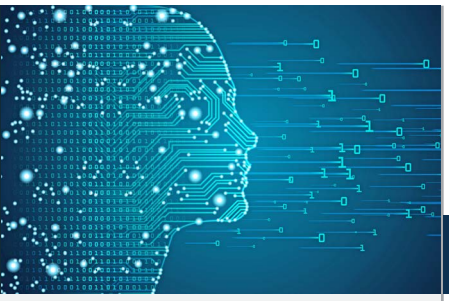

Bio-Algorithms and Med-Systems

WWW.BAMSJOURNAL.COM ISSN: 1896-530X

ORIGINAL ARTICLE

Received: 30.08.2024
Accepted: 21.10.2024
Published: 21.11.2024

CITE THIS ARTICLE AS:
Ardebili FT, Moskal P, on behalf of the J-PET collaboration, "Assessing the Spatial Resolution of the Modular J-PET Scanner using the Maximum-Likelihood Expectation--Maximization (MLEM) algorithm," Bio-Algorithms and Med-Systems vol. 20, special issue, pp. 1-9, 2024, DOI: 10.5604/01.3001.0054.8095

AUTHORS' CONTRIBUTION:
A. Conceptualization
B. Data Curation
C. Formal Analysis
D. Funding Acquisition
E. Investigation
F. Methodology
G. Project Administration
H. Resources
I. Software
J. Supervision
K. Validation
L. Visualization
M. Writing – Original Draft
N. Writing – Review & Editing

CORRESPONDING AUTHOR:
Faranak Tayefi Ardebili; M. Smoluchowski Institute of Physics, Faculty of Physics, Astronomy and Applied Computer Science, Jagiellonian University, Krakow, Poland; 11 Łojasiewicza St., 30-348 Kraków, Poland; Phone: +48 510399372;
E-mail: faranaktayefi.tayefi.ardebili@doctoral.uj.edu.pl

Assessing the Spatial Resolution of the Modular J-PET Scanner using the Maximum-Likelihood Expectation-Maximization (MLEM) algorithm

Faranak Tayefi Ardebili[1,2,3BCEFIKLM], **Paweł Moskal**[1,2,3ADGEFHJKN], **on behalf of the J-PET collaboration**

[1]M. Smoluchowski Institute of Physics, Faculty of Physics, Astronomy and Applied Computer Science, Jagiellonian University, Krakow, Poland
[2]Total-Body Jagiellonian-PET Laboratory, Jagiellonian University, Krakow, Poland
[3]Center for Theranostics, Jagiellonian University, Krakow, Poland

ABSTRACT

Introduction: The presented study evaluates the spatial resolution of the Modular J-PET scanner using the National Electrical Manufacturers Association (NEMA) NU2-2018 standard. The Modular J-PET, constructed with BC-404 plastic scintillators in an axial arrangement and coupled with analogue Silicon Photomultipliers (SiPMs) at both ends, offers a 50 cm axial field of view and a bore diameter of 73.9 cm. The study compares results from GATE simulations with experimental data.

Objective: The primary objective of this study is to assess the spatial resolution of the Modular J-PET scanner, using Time-of-Flight (TOF) and non-TOF image reconstruction, based on NEMA NU2-2018 guidelines.

Methods: Spatial resolution was evaluated using a Na-22 point-like source as recommended by NEMA NU2-2018. Both TOF and non-TOF list mode acquisitions were performed, with a comparative analysis of the results from experimental and simulated data.

Results: Radial spatial resolution, obtained based on the experimental data when taking into account TOF, is equal to 4.92 ± 0.56 mm, 7.38 ± 0.49 mm, and 6.94 ± 0.38 mm at positions 1 cm, 10 cm, and 20 cm from the detector centre, respectively. The tangential spatial resolution for TOF image reconstruction was determined as 7.38 ± 0.51 mm, 7.37 ± 0.10 mm, and 14.67 ± 0.31 mm at the same positions based on experimental data, while axial spatial resolution was calculated as 30.73 ± 0.52 mm, 30.73 ± 0.64 mm, and 31.96 ± 0.29 mm based on experimental data. Simulated radial spatial resolution for TOF image reconstruction methods was found to be 4.80 ± 0.59 mm, 7.26 ± 0.55 mm, and 6.67 ± 0.42 mm at positions 1 cm, 10 cm, and 20 cm from the detector centre, respectively. The simulated tangential spatial resolution for TOF image

reconstruction methods was determined as 7.27 ± 0.47 mm, 7.27 ± 0.59 mm, and 15.1 ± 0.4 mm at the corresponding positions, while the simulated axial spatial resolution was determined as 29.97 ± 0.49 mm, 30.53 ± 0.74 mm, and 31.78 ± 0.11 mm. **Conclusions:** The Modular J-PET meets NEMA NU2-2018 standards, with TOF mode providing better spatial resolution than non-TOF, validating the system's high--resolution imaging capabilities.

KEYWORDS

positron emission tomography, plastic scintillator, spatial resolution, GATE simulation, medical imaging

LIST OF ABBREVIATIONS

AFOV – axial field of view
DAQ – Data Acquisition System
DOI – depth of the interaction
ESR – Enhanced Specular Reflector
FBP – Filtered Back Projection
FOV – Field of View
FPGA – Field-Programmable Gate Array
FWHM – full width at half-maximum
GATE – Geant4 Application for Tomographic Emission
LAFOV – longer axial field of view
LM – List-Mode
LOR – Line of Response
MLEM – maximum likelihood expectation maximization algorithm
NEMA – the National Electrical Manufacturers Association
PET – Positron Emission Tomography
PSF – point spread functions
QETIR – Quantitative Emission Tomography Iterative Reconstruction
SiPMs – Silicon Photomultipliers
TOF – Time-of-Flight
WLS – wavelength shifter

INTRODUCTION

Positron Emission Tomography (PET) plays a fundamental role in the clinical diagnosis of cancer [1]. This imaging modality is at the forefront of detecting oncological abnormalities, offering unparalleled insights into tumour biology and facilitating early diagnosis and effective treatment planning. PET imaging operates by utilising radiotracers which, upon injection, emit positrons that interact with electrons in the body, resulting in the emission of gamma rays. These gamma rays are detected by the PET scanner, creating detailed images of the metabolic activity within the body [2–4]. The axial field of view (AFOV) in conventional PET scanners typically ranges from 15 to 26 cm [5, 6]. Whole-body scans of patients usually require multiple bed positions due to the limited AFOV, which, depending on the patient's size, can take from 10 to 20 minutes [1, 4]. One effective strategy to enhance sensitivity and reduce scan duration is to extend the AFOV [7–9]. A longer axial field of view (LAFOV) allows for the acquisition of whole--body imaging data in a single bed position, significantly reducing the acquisition time compared to conventional PET scanners [10].

The uExplorer PET system, with an AFOV of 194.6 cm, is the world's first Total-Body tomograph, developed at UC Davis, California [11]. While Total-Body PET scanners offer significant advantages over conventional tomographs, their worldwide utilisation has been limited due to the high construction cost per unit. However, the benefits of Total-Body PET systems have driven significant research within the molecular imaging community to develop more affordable alternatives.

The J-PET collaboration at Jagiellonian University is one of the pioneers in developing cost-effective alternatives for LAFOV PET scanners [9, 12], enabling positronium and quantum entanglement imaging [13–15], as well as basic physics experiments [16, 17]. J-PET technology uses plastic scintillators in a unique axial arrangement of the detectors, reducing the need for silicon photomultipliers (SiPM) and the corresponding electronics [18–21]. This cost reduction is estimated to be approximately five times lower than that of current crystal-based PET tomographs [12]. The Modular J-PET is the most recent prototype from this collaboration. This scanner, providing a 50 cm AFOV, offers 2–3 times larger AFOV compared to conventional PET scanners at a considerably lower construction cost. The unique technology utilised in the construction of these tomographs allows users to reconfigure the detector arrangements based on their needs, thanks to its modular design [13–24].

Determining the performance characteristics of the Modular J-PET is essential for evaluating its potential for clinical use in hospitals [25]. The National Electrical Manufacturers Association (NEMA) provides standards that ensure the quality of measurement results and enable the comparison of performance characteristics among different PET systems [26]. The NEMA NU2-2018 standards outline a specific protocol for evaluating the system characteristics of PET scanners, such as spatial resolution, scatter fraction, count

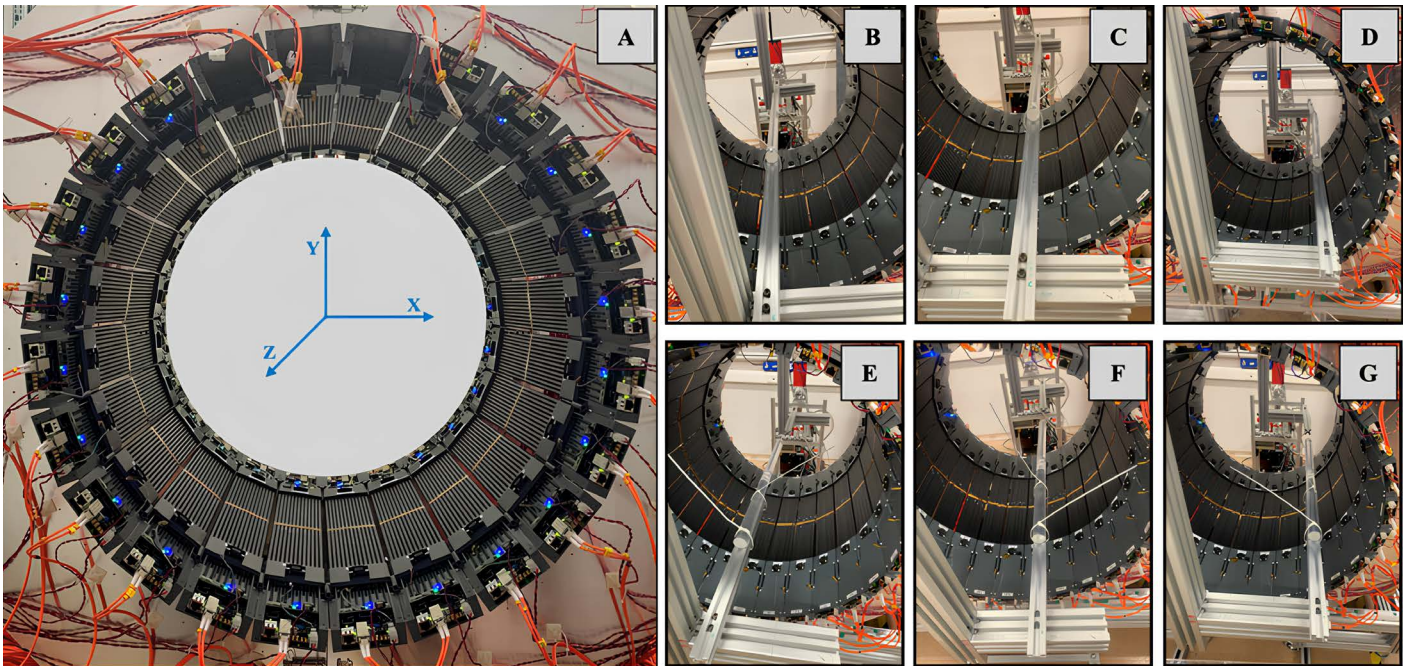

Fig. 1. (A) The Modular J-PET scanner, featuring 24 individual modules with a total weight of approximately 2 kg per each module; (B–G) The ^{22}Na point-like source positioned in the poly(methyl methacrylate) at various locations: (B) (1,0,0) cm, (C) (10,0,0) cm, (D) (20,0,0) cm, (E) (1,0,18.75) cm, (F) (10,0,18.75) cm, and (G) (20,0,18.75) cm.

losses, sensitivity, and image quality [26]. The sensitivity of the Modular J-PET has been discussed in previous studies [21].

The main aim of this study is to investigate the spatial resolution of the Modular J-PET based on the NEMA NU2-2018 standards. The experimental results have been cross-validated using Monte Carlo simulations performed with the use of GATE software.

METHOD

Design of the Modular J-PET

The Modular J-PET represents the latest prototype developed by the J-PET collaboration, serving as the most recent iteration on the path to constructing a total-body J-PET [27]. The Modular J-PET scanner comprises 24 individual detection units, configured in a regular 24-sided polygon that circumscribes a cylinder with a diameter of 73.9 cm, as illustrated in Fig. 1. [21, 28, 29]. Each module consists of 13 BC-404 rectangular plastic scintillator strips, being 6 mm × 24 mm in cross section, 50 cm in length, and positioned parallel to the axial axis of the scanner. To improve light propagation and prevent leakage, the plastic scintillator strips are wrapped in Vikuiti Enhanced Specular Reflector (ESR) foil and DuPont Kapton 100B film [30–32]. Each plastic scintillator is read out by four Hamamatsu S13 Silicon Photomultipliers (SiPMs) at each end, featuring an active area of 6 mm x 6 mm and 1 x 4 array. Each SiPM is equipped with two threshold settings: 30 mV and 70 mV. Upon the interaction of gamma quanta with a scintillator strip, four timestamps are generated across the eight SiPMs. These timestamps are continuously collected by the Data Acquisition System (DAQ) via the front-end electronics. The DAQ system in the Modular J-PET uses Field-Programmable Gate Array (FPGA) electronics for efficient real-time processing of multiple data streams through pipelined operations [33]. The modular J-PET was used to demonstrate the first positronium image of the human brain [14].

Monte Carlo Simulation of the Modular J-PET

In parallel with the experimental measurement, the study has been simulated to evaluate the spatial resolution of the Modular J-PET under ideal conditions. For this purpose, Geant4 Application for Tomographic Emission (GATE) software (version 9.0) [34–38], which is a validated toolkit in nuclear medicine and molecular imaging, has been utilised. The Modular J-PET scanner was simulated with the exact dimensions of the experimental system as described in sub-section “A” of Method [39, 40].

Image analysis and processing

The image reconstruction process employed the Quantitative Emission Tomography Iterative Reconstruction (QETIR) software, which uses an iterative list-mode maximum likelihood expectation maximization (MLEM) algorithm [41]. This tool works with both Time-of-Flight (TOF) and non-TOF List-Mode (LM) data, which can be transformed into TOF or non-TOF sinograms as needed. A key feature of the QETIR software is its ability to generate a sensitivity correction map independently. To create this map, users must initiate a configuration process that involves setting parameters such as a sensitivity map size of 200 mm × 200 mm × 200 mm, voxel dimensions of 2.5 mm × 2.5 mm × 2.5 mm, and the number of back-to-back photons per voxel at 20,000, along

with other necessary details. The TOF value (σ) used for image reconstruction was 267 ps, determined based on experimental measurements [42].

Spatial resolution

Spatial resolution in PET systems refers to their ability to differentiate between two separate emission points after image reconstruction [26]. This measurement aims to describe the widths of the reconstructed image point spread functions (PSF) of small radioactive sources (NEMA standards). The width of the PSF is quantified by its full width at half-maximum (FWHM). Spatial resolution in PET is evaluated using a ^{22}Na point source. According to NEMA standards, six specific positions are defined for placing the source inside the detector: In the axial direction, these positions include the centre of the axial Field of View (FOV) and three-eighths of the FOV from the centre. In the transverse direction, the positions are 1 cm, 10 cm, and 20 cm away from the centre of the detector plane. The positioning accuracy in the transaxial plane is specified as 2 mm for 1 cm and 5 mm for both 10 cm and 20 cm. Axial positioning accuracy is also set at 2 mm. To ensure the reliability of the spatial resolution data, a minimum of 100,000 counts must be acquired at each of the six positions. Following the reconstruction and generation of images for each position, each image was analysed on a bin--by-bin basis [26, 42]. A line profile was extracted through the distribution peak in three orthogonal directions, adhering to NEMA standards. The FWHM for each point was calculated by first determining the maximum value of each line profile through a parabolic fit of the peak point and its two nearest neighbours. Subsequently, the FWHM was computed via linear interpolation between adjacent bins at half of this maximum value. This method involved performing linear interpolation between consecutive bins, using calculations based on the midpoint values of bins on both the left and right sides of the distribution [21].

Spatial resolution measurement

A 9.2 MBq ^{22}Na point-like source was employed to assess the spatial resolution of the Modular J-PET scanner [26, 43]. The ^{22}Na isotope was encased in a stainless steel cylinder with an outer diameter of 4.76 mm and a height of 5.72 mm, featuring an active diameter of 3.18 mm. To position the steel cylinder within the detector, a poly(methyl methacrylate) was used. This cylinder was precisely placed at the centre of the poly(methyl methacrylate), as illustrated in Fig. 2. [42]. Locating the poly(methyl methacrylate) within the scanner required the use of aluminium supports, as explicitly shown in Fig. 1. Due to the length of the poly(methyl methacrylate), these aluminium supports were situated outside the detector's AFOV. A 1-hour measurement was conducted for each source position. Fig. 1. depicts the point-like source within the poly(methyl methacrylate) in different positions inside the Modular J-PET.

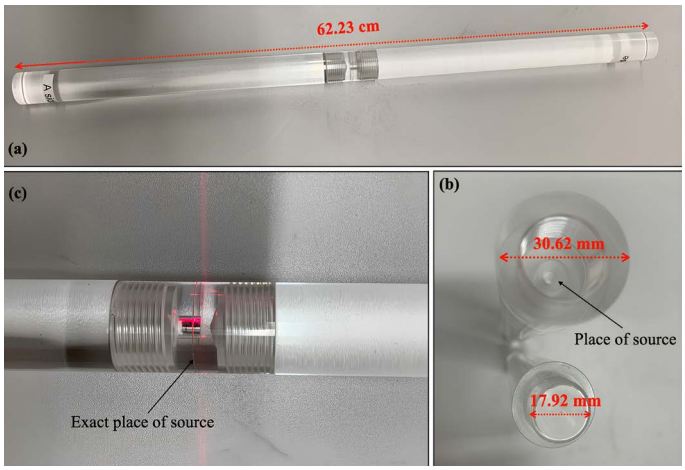

Fig. 2. (A) Illustrates the poly(methyl methacrylate) used for spatial resolution measurement, with a length of 62.23 cm and an outer diameter of 30.62 mm; (B) Cross-section of the middle of the poly(methyl methacrylate), showing the source positioned at the centre; (C) Placement of the point-like source within the poly(methyl methacrylate), with the line indicating the exact location of the source inside the rod. To aid in visually identifying the exact location of the source within the rod, a prominent line was incorporated into the rod's design.

Spatial resolution simulation

To assess spatial resolution, a ^{22}Na point-like source, measuring 0.5 cm in diameter and containing 9.2 MBq of activity, was simulated. This source was encased in an aluminium cylinder with a length of 0.58 cm and a diameter of 0.5 cm, as depicted in Fig. 3. Simulations were conducted at six different positions. The activity and position of the source inside the detector were selected according to our experimental measurements. Fig. 3. illustrates a schematic representation of the spatial resolution of the point-like source within the detector.

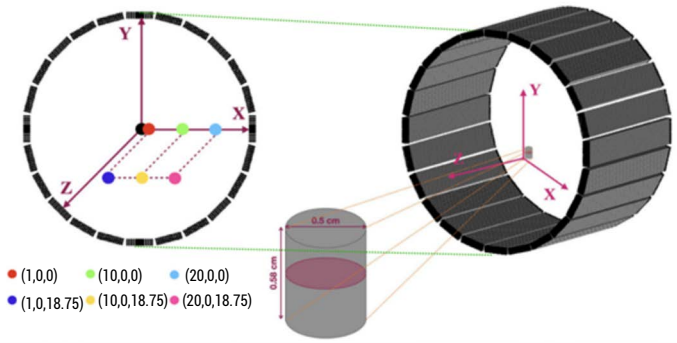

Fig. 3. (Right) GATE visualisation of the Modular J-PET scanner and an example of the ^{22}Na source inside the aluminium cylinder positioned at (1, 0, 0) cm. The ^{22}Na source is entered within the aluminium phantom, with the active area forming a circular plane at half the phantom's length; (Left) Schematic illustration of source positions within the Modular J-PET, with the black dot indicating the centre of the detector. Note that the figure is not drawn to scale. Position measurements are given in cm.

Tab. I. FWHM values and their uncertainties (in mm) for various positions from experimental data and simulation data, comparing TOF and non-TOF image reconstruction methods. Radial FWHM corresponds to values along the X-axis, tangential FWHM to values along the Y-axis, and axial FWHM to values along the Z-axis. All results are based on the first iteration.

		EXPERIMENTAL DATA			SIMULATION DATA		
Source position (cm)		Radial FWHM (mm)	Tangential FWHM (mm)	Axial FWHM (mm)	Radial FWHM (mm)	Tangential FWHM (mm)	Axial FWHM (mm)
(1,0,0)	TOF	4.92 ± 0.55	7.38 ± 0.54	29.50 ± 0.52	4.80 ± 0.45	7.27 ± 0.25	29.05 ± 0.54
(10,0,0)		4.92 ± 0.13	7.38 ± 0.10	27.04 ± 0.51	4.80 ± 0.54	7.27 ± 0.66	27.00 ± 0.89
(20,0,0)		6.50 ± 0.40	12.13 ± 0.30	29.50 ± 0.30	6.08 ± 0.74	12.37 ± 0.82	29.50 ± 0.94
(1,018.75)		4.92 ± 0.57	7.38 ± 0.49	31.96 ± 0.52	4.80 ± 0.12	7.27 ± 0.41	30.89 ± 0.44
(10,018.75)		9.83 ± 0.69	7.37 ± 0.10	34.42 ± 0.75	9.73 ± 0.56	7.27 ± 0.39	34.06 ± 0.58
(20,018.75)		7.38 ± 0.37	17.21 ± 0.32	34.43 ± 0.28	7.27 ± 0.11	17.83 ± 0.14	34.06 ± 0.13
(1,0,0)	non-TOF	4.92 ± 0.12	7.38 ± 0.11	34.42 ± 0.10	4.81 ± 0.11	7.27 ± 0.54	34.75 ± 0.36
(10,0,0)		4.92 ± 0.30	7.38 ± 0.228	31.83 ± 0.56	4.81 ± 0.14	7.27 ± 0.207	31.62 ± 0.611
(20,0,0)		6.50 ± 0.09	12.50 ± 0.07	35.00 ± 0.09	6.70 ± 0.09	12.75 ± 0.90	34.50 ± 0.94
(1,018.75)		4.92 ± 0.00	7.38 ± 0.12	34.42 ± 0.13	4.81 ± 0.21	7.27 ± 0.94	35.00 ± 0.65
(10,018.75)		9.83 ± 0.17	7.21 ± 0.10	34.42 ± 0.20	9.73 ± 0.19	7.27 ± 0.50	34.96 ± 0.218
(20,018.75)		7.53 ± 0.10	14.42 ± 0.10	35.00 ± 0.09	7.38 ± 0.11	15.83 ± 0.16	34.75 ± 0.26

Event selection criteria

The collected data from the experimental measurements were analysed using the J-PET framework, a specialised tool based on the C++ language. To achieve high-quality reconstructed images, it is crucial to remove background elements, such as scatter and random coincidence events, from the dataset [20]. All event selection criteria are comprehensively explained in [21, 42]. It is important to note that all event selection criteria were also applied to the simulation. The response of the SiPMs was not directly simulated; instead, it was assumed that the system inherently possesses a time resolution (sigma) of 267 ps and an energy resolution of 0.23% at 340 keV. Additionally, a 20 ns dead time was incorporated into the simulation, reflecting the electronic characteristics of the Modular J-PET [42].

RESULTS

Image reconstruction has been analysed by the AMIDE software to determine the precise source positions. Fig. 4. displays the

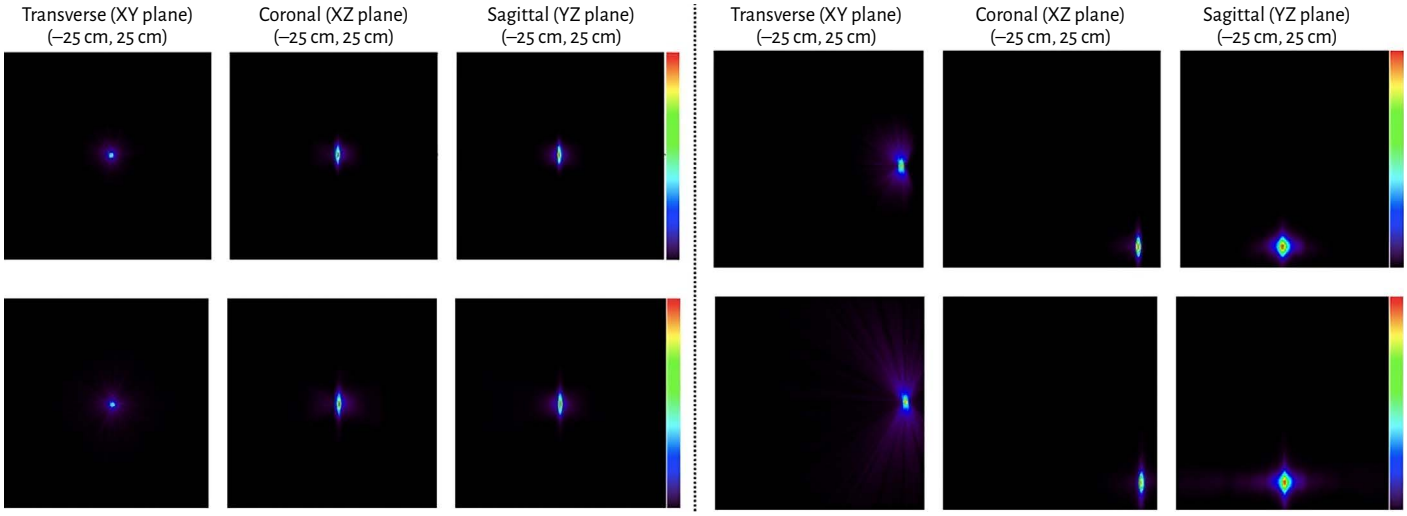

Fig. 4. (Top row) Results of image reconstruction using TOF List Mode data; (Bottom row) Results of image reconstruction using non-TOF List Mode data. The images shown were obtained from the first iteration and show the reconstructed images in three directions for two positions: (1,0,0) (left side) and (20,0,18.75) (right side). The vertical color scales are arbitrary units, scaled from 0 to 1.

reconstructed images from the experimental data in three directions, generated using the QETIR software for both TOF and non-TOF List Mode data, at positions (1,0,0) cm and (20,0,18.75) cm. These positions were chosen due to their significance: (1,0,0) cm is near the centre of the Modular J-PET, while (20,0,18.75) cm is close to the edge of the scanner.

Subsequently, a line profile was extracted from each image in three directions. The FWHM and their corresponding uncertainties were computed using the NEMA norm methods for all positions and are tabulated in Tab. I. The images and results presented are derived from the first iteration of each reconstruction, making them more comparable with the results obtained from Filtered Back Projection (FBP) [44–46]. Tab. I. also displays the FWHM and its corresponding uncertainty estimation for the distribution along the three directions was determined for all positions at the simulation level, accounting for a hit position uncertainty of 15.0 mm along the Z-axis. Fig. 5. shows the images generated by the QETIR software for the position (1,0,0) for both TOF and non--TOF methods at the simulation level.

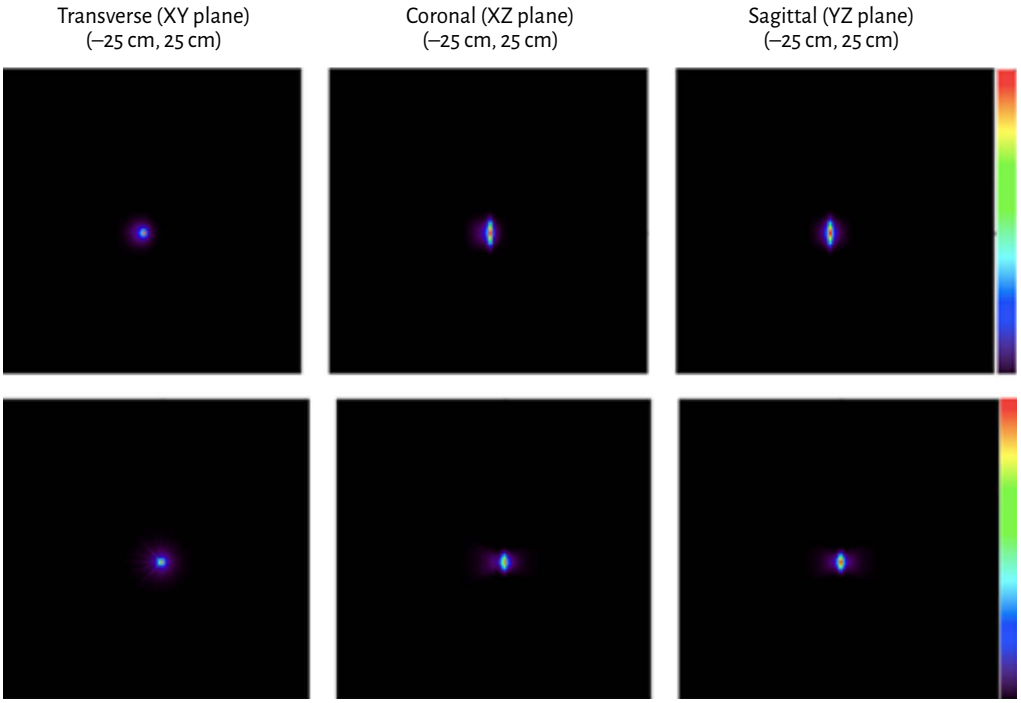

Fig. 5. The outcomes of image reconstruction for the source positioned at (1,0,0) from the simulation: (Top row) generated using TOF List Mode data; (Bottom row) generated using non-TOF List Mode data. The images shown were obtained from the first iteration and showcase the reconstructed image in three directions. The vertical color scales are arbitrary units, scaled from 0 to 1.

Since iterative algorithms were used to calculate spatial resolution, reconstructions were performed over 10 iterations with 1 subset. The FWHM results in the three directions for the position (1, 0, 0), using both TOF and non-TOF image reconstruction methods, are displayed in Fig. 6. for the experimental data.

DISCUSSION

The study aimed to investigate the spatial resolution of the Modular J-PET scanner following the NEMA NU2-2018 guidelines. As shown in Tab. I., the FWHM value along the y-axis exceeds that along the x-axis. This discrepancy is primarily due to the dimensions of the plastic scintillators, which measure 6 mm × 24 mm, leading to increased uncertainty in the depth of the interaction (DOI). The greatest challenge in achieving good spatial resolution occurs along the z-axis, which is influenced by the specific geometry of the Modular J-PET detector. The unique design and structure of the detector significantly impact spatial resolution, highlighting the inherent difficulties in achieving uniform resolution across all axes. Enhancing spatial resolution along axial axes, in longer AFOV versions of the J-PET scanners, is feasible through the use of a wavelength shifter (WLS). Employing WLS can improve axial spatial resolution in plastic scintillators, offering a means to achieve more consistent and precise imaging [47].

The results presented in Tab. I. demonstrate that TOF list mode provides superior spatial resolution. Integrating TOF information into the PET reconstruction markedly improves image quality. TOF data enables more precise estimation of emission points

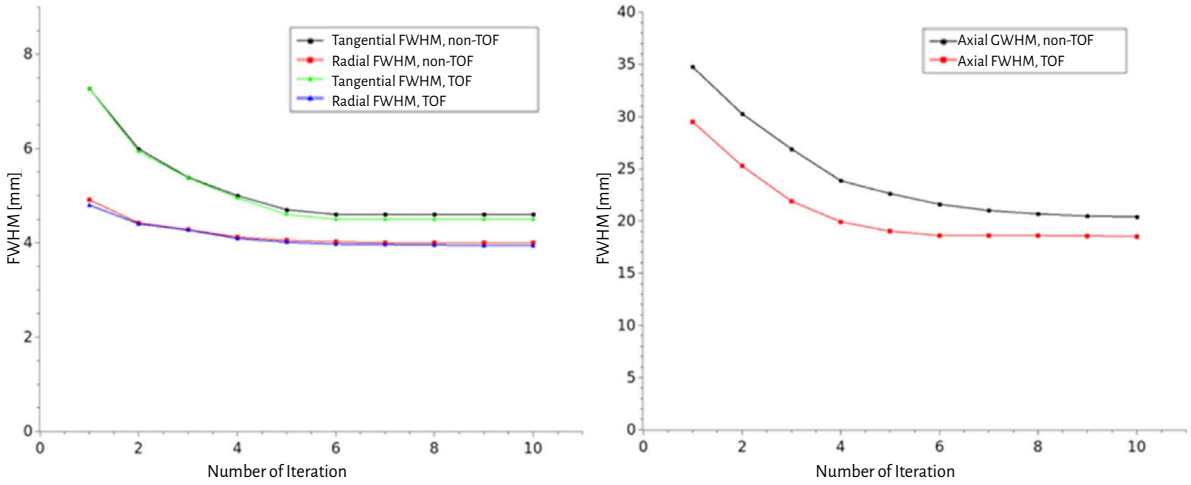

Fig. 6. FWHM values *versus* number of iteration for the (1,0,0) position in three directions from the experimental data – (Left) Radial and tangential FWHM using TOF and non-TOF image reconstruction methods; (Right) Axial FWHM using TOF and non-TOF image reconstruction methods.

along each Line of Response (LOR) during the reconstruction process. Instead of updating image voxels along the entire LOR, updates are restricted to specific segments determined by the TOF resolution. This approach reduces the interdependence between image voxels, thereby minimising noise propagation. As a result, the method facilitates faster and more consistent convergence, enhancing lesion detection capabilities.

To validate the experimental results, a Monte Carlo model of the Modular J-PET scanner was employed using the GATE simulation platform. The simulation results, using the same point-like source at the specified positions, showed good agreement with the experimental findings, with discrepancies of less than 1.41 mm. Variations between the simulation and experimental results can be attributed to differences in experimental and simulation conditions, such as the digitizer, light transport between crystals, and SiPM characteristics, which were not fully accounted for in the simulation study.

CONCLUSIONS

The objectives of this work were to estimate the spatial resolution of the Modular J-PET system studied in accordance with the NEMA NU2-2018 standard, utilising the MLEM algorithms. Additionally, the system was modelled using the GATE Monte Carlo toolkit. The results demonstrated good agreement, with minor differences attributed to the absence of poly(methyl methacrylate) simulations during the simulation phase. This study also presents a comparison between TOF and non-TOF list mode data. The findings indicate that images generated using TOF list mode exhibit higher quality and improved spatial resolution. Specifically, the FWHM and their uncertainties with TOF list mode for the position (1,0,0) cm were 4.92 ± 0.56 mm in the radial direction, 7.38 ± 0.54 mm in the tangential direction, and 29.50 ± 0.52 mm in the axial direction. Similarly, for simulation data at the position (1,0,0) cm, the FWHM values were 4.80 ± 0.45 mm in the radial direction, 7.27 ± 0.25 mm in the tangential direction, and 29.05 ± 0.54 mm in the axial direction. It is noteworthy that the tangential and radial spatial resolution values of the Modular J-PET detector are comparable to those of commercial PET devices. Future enhancements are anticipated to improve axial spatial resolution by expanding the axial field of view of the scanner and implementing WLS techniques [13, 48].

ACKNOWLEDGEMENTS AND FUNDING

We acknowledge support from the National Science Center of Poland through Grants No. 2021/42/A/ST2/00423, 2021/43/B/ST2/02150, Jagiellonian University via Project No. CRP/0641.221.2020, and the SciMat and qLife Priority Research Area budget under the auspices of the program Excellence Initiative – Research University at Jagiellonian University.

REFERENCES

1. Vandenberghe S, Moskal P, Karp JS. State of the art in total body PET. EJNMMI Phys. 2020;7(1):35.
2. Alavi A, Werner T, Stepien E, Moskal P. Unparalleled and revolutionary impact of PET imaging on research and day to day practice of medicine. Bio-Algorithms and Med-Systems. 2021;17:203-12.
3. Alavi A, Saboury B, Nardo L, Zhang V, Wang M, Li H, et al. Potential and most relevant applications of total body PET/CT imaging. Clin Nucl Med. 2022;47:43-55.
4. Surti S, Pantel AR, Karp JS. Total Body PET: Why, How, What for?. IEEE Trans Radiat Plasma Med Sci. 2020;4(3):283-92.
5. Zhang X, Zhou J, Cherry SR, Badawi RD, Qi J. Quantitative image reconstruction for total-body PET imaging using the 2-meter long EXPLORER scanner. Phys Med Biol. 2017;62(6):2465-85.
6. Nadig V, Herrmann K, Mottaghy FM, Schulz V. Hybrid total-body pet scanners-current status and future perspectives. Eur J Nucl Med Mol Imaging. 2022;49:445-59.
7. Cherry SR, Jones T, Karp JS, Qi J, Moses WW, Badawi RD. Total-body PET: maximising sensitivity to create new opportunities for clinical research and patient care. J. Nucl. Med. 2018;59(1):3-12.
8. Surti S, Karp J. Impact of detector design on imaging performance of a long axial field-of-view, whole-body PET scanner. Phys Med Biol. 2015;60(13):5343-58.
9. Moskal P, Kowalski P, Shopa RY, Raczyński L, Baran J, Chung N, et al. Simulating NEMA characteristics of the modular total-body J-PET scanner – an economic total-body PET from plastic scintillators. Phys. Med. Biol 2021;66:175015.
10. Rezaei H, Sheikhzadeh P, Ghafarian P, Zaidi H, Ay MR. Accurate modeling and performance evaluation of a total-body pet scanner using Monte Carlo simulations. Med Phys. 2023;50(11):6815-27.
11. Spencer BA, Berg E, Schmall JP, Omidvari N, Leung EK, Abdelhafez YG, et al. Performance evaluation of the uExplorer total-body PET/CT scanner based on NEMA-nu 2-2018 with additional tests to characterize pet scanners with a long axial field of view. J. Nucl. Med. 2021;61:861.
12. Moskal P, Stepien E. Prospects and clinical perspectives of total-body PET imaging using plastic scintillator. PET Clinics. 2020;15:439-52.
13. Moskal P, Dulski K, Chug N, Curceanu C, Czerwiński E, Dadgar M, et al. Positronium imaging with the novel multi-photon PET scanner. Sci Adv. 2021;7:eabh4394.
14. Moskal P, Baran J, Bass S, Choiński J, Chug N, Curceanu C, et al. First positronium image of the human brain in vivo. Sci Adv. 2024;10(37):adp2840.
15. Moskal P, Kumar D, Sharma S, Beyene EY, Chug N, Coussat A, et al. Non-maximal entanglement of photons from positron-electron annihilation demonstrated using a novel plastic PET scanner. HEP 2024;arXiv:2407.08574.
16. Moskal P, Czerwiński E, Raj J, Bass SD, Beyene EY, Chug N, et al. Discrete symmetries tested at 10^-4 precision using linear polarization of photons from positronium annihilations. Nat Commun. 2024;15(1):78.
17. Moskal P, Gajos A, Mohammed M, Chhokar J, Chug N, Curceanu C, et al. Testing CPT symmetry in ortho-positronium decays with positronium annihilation tomography. Nat Commun. 2021;12(1):5658.
18. Moskal P, Niedźwiecki S, Bednarski T, Czerwiński E, Kapłon Ł, Kubicz E, et al. Test of a single module of the J-PET scanner based on plastic scintillators. Nucl. Instrum. Methods Phys. Res 2014;764:317-28.
19. Sharma S, Povolo L, Mariazzi S, Korcyl G, Kacprzak K, Kumar D, et al. Feasibility studies for imaging e+e- annihilation with modular multi-strip detectors. Nucl. Instrument. Meth. 2024;1062:169192.
20. Kowalski P, Wiślicki W, Raczyński L, Alfs D, Bednarski T, Białas P, et al. Scatter fraction of the J-PET tomography scanner. Acta Phys. Polon. B 2016;47:549.
21. Ardebili FT, Niedźwiecki S, Moskal P. Evaluation of Modular J-PET sensitivity. Bio-Algorithms and Med-Systems 2023;19:132-8.
22. Niedźwiecki S, Białas P, Curceanu C, Czerwiński E, Dulski K, Gajos A, et al. J-PET: a new technology for the whole-body PET imaging. Acta Physica Polonica B. 2017;48:1567-70.
23. Moskal P, Kisielewska D, Curceanu C, Czerwiński E, Dulski K, Gajos A, et al. Feasibility study of the positronium imaging with the J-PET tomograph. Phys. Med. Biol 2019;64:055017.
24. Moskal P, Jasińska B, Stępień E, Bass SD. Positronium in Medicine and Biology. Nat. Rev. Phys. 2019;1(9):527-9.
25. nist.gov [Internet]. National Institute of Standards and Technology; 2020 [cited 2021 March 24]. Available from: https://nist.gov/pml.
26. NEMA Standards Publication NU 2-2018: Performance Measurements of Positron Emission Tomographs. National Electrical Manufacturers Association. Rosslyn VA, USA, 2018.
27. Dadgar M, Parzych S, Ardebili FT. A Simulation Study to Estimate Optimum LOR Angular Acceptance for the Image Reconstruction with the Total-Body J-PET. MIUA 2021;12:189-200.
28. Dadgar M, Kowalski P. GATE Simulation Study of the 24-Module JPET Scanner: Data Analysis and Image Reconstruction. Acta Phys. Pol. B. 2020;51:309-11.
29. Kapłon L, Moskal G. Blue-emitting polystyrene scintillators for plastic scintillation dosimetry. Bio-Algorithms and Med-Systems 2021;17(3):191-7.
30. 3M.com [Internet]. Science. Applied to Life; [cited 2021 March 24]. Available from: https://www.3m.com.
31. dupont.com [Internet]; [cited 2021 March 24]. Available from: https://www.dupont.com.
32. Kaplon L. Technical Attenuation Length Measurement of Plastic Scintillator Strips for the Total-Body J-PET Scanner. IEEE Trans. Nucl. Sci. 2020;67(10):2286-9.
33. Korcyl G, Białas P, Curceanu C, Czerwiński E, Dulski K, Flak B, et al. Evaluation of single-chip, real-time tomographic data processing on fpga soc devices. IEEE Transactions on Medical Imaging 2018;37:2526-35.
34. Jan S, Santin G, Strul D, Staelens S, Assié K, Autret D, et al. GATE – Geant4 Application for Tomographic Emission: a simulation toolkit for PET and SPECT. Phys. Med. Biol. 2004;49(19):4543-61.
35. Jan S, Benoit D, Becheva E, Carlier T, Cassol F, Descourt P, et al. GATE V6: a major enhancement of the GATE simulation platform enabling modelling of CT and radiotherapy. Phys. Med. Biol. 2011;56(4):881.
36. Sarrut D, Bała M, Bardies M, Bert J, Chauvin M, Chatzipapas K, et al. Advanced Monte Carlo simulations of emission tomography imaging systems with GATE. Phys. Med. Biol 2021;66(10):10TR03.
37. Agostinelli S, Allison J, Amako K, Apostolakis J, Araujo H, Arce P, et al. Geant4 – a simulation toolkit. Nucl. Instrum. Methods Phys. Res. A. 2003;506(3):250-303.

38. Kowalski P, Raczyński L, Bednarski T, Białas P, Czerwiński E, Giergiel K, et al. Determination of the map of efficiency of the Jagiellonian Positron Emission Tomograph (J-PET) detector with the GATE package. Bio-Algorithms and Med-Systems 2014;10(2):85-90.

39. Allison J, Amako K, Apostolakis J, Arce P, Asai M, Aso T, et al. Recent developments in GEANT4. Nucl. Instrum. Methods Phys. Res. A. 2016;835:186-225.

40. eljentechnology.com [Internet]. Physical Constants Of Plastic Scintillators; [cited 2021 March 24]. Available from: https://eljentechnology.com/images/technical/_library/Physical-Constants-Plastic.pdf.

41. Dadgar M. Feasibility study of lesion detection by means of total-body jagiellonian positron emission tomography scanner [dissertation]. Krakow: Jagiellonian University; 2022.

42. Tayefi Ardebili TF. Evaluation of the NEMA characteristics for the Modular J-PET scanner [dissertation]. Krakow: Jagiellonian University; 2024.

43. Gonzalez-Montoro A, Sánchez F, Bruyndonckx P, Cañizares G, Benlloch JM, González AJ. Novel method to measure the intrinsic spatial resolution in PET detectors based on monolithic crystals. Nucl. Instrum. Methods Phys. Res. A. 2019;920:58-67.

44. Ermert J, Neumaier B. The Radiopharmaceutical Chemistry of Fluorine-18: Nucleophilic Fluorinations. In: Lewis J, Windhorst A, Zeglis B, editors. Radiopharmaceutical Chemistry. Cham: Springer; 2019. p. 273-83.

45. Schmall JP, Karp JS, Werner M, Surti S. Parallax error in long-axial field-of-view PET scanners – a simulation study. Phys Med Biol. 2016;61(14):5443-55.

46. Suljic A, Tomse P, Jensterle L, Skrk D. The impact of reconstruction algorithms and time of flight information on PET/CT image quality. Radiol Oncol. 2015;49(3):227-33.

47. Dadgar M, Parzych S, Baran J, Chug N, Curceanu C, Czerwiński E, et al. Comparative studies of the sensitivities of sparse and full geometries of Total-Body PET scanners built from crystals and plastic scintillators. EJNMMI Physics 2023;10(62):2304.05834.

48. Smyrski J, Alfs D, Bednarski T, Białas P, Czerwiński E, Dulski K, et al. Measurement of gamma quantum interaction point in plastic scintillator with WLS strips. Nucl. Instrument. Meth. A. 2017;851:39-42.